J Adv Ceram

Research Article

Lead-free multilayer ceramic capacitors featuring ultrahigh remanent polarization and excellent thermal stability for high-power force-electric energy conversion

Maocai Xu[1,2], Meng Xie[2,✉], Min Shi[2], Mingyue Ge[3], Shiyu Fang[4], Hao Hong[2], Tengfei Hu[2], Zimeng Hu[2], Fei Cao[2], Anwei Sun[5], Jia Yang[5], Zhengwei Xiong[3], Xujie Lv[4], Zhipeng Gao[3,5], Hengchang Nie[1,2,6,✉], Genshui Wang[1,2,6,✉]

Cite this article: Xu M, Xie M, Shi M, et al. *J Adv Ceram* 2026, **15**(8): 9221345. https://doi.org/10.26599/JAC.2026.9221345

ABSTRACT: The ever-growing global energy demand has driven a surge of research interest in the field of energy harvesting and conversion. Among them, high-power force-electric energy conversion devices based on charge storage via the polarization effect of ferroelectric (FE) materials have attracted considerable interest for specialized applications owing to their advantages of long shelf life, ultrafast response, and high current/voltage output. Nevertheless, the primary bottleneck hindering the development and practical deployment of such energy storage systems lies in the low remanent polarization (P_r) and insufficient thermal stability of most state-of-the-art lead-free ferroelectric materials. In this work, a synergistic optimization strategy of composition-driven structural distortions and defect-induced pinning effects via silver niobate (AN) and $MnCO_3$ doping is applied to bismuth sodium titanate (BNT)-based ferroelectric ceramics. The optimized $0.98Bi_{0.5}Na_{0.5}TiO_3$–$0.02AgNbO_3$–0.20 wt% $MnCO_3$ lead-free ferroelectric ceramics exhibit significantly enhanced P_r and thermal stability, achieving an ultrahigh P_r of 52.21 μC/cm² and excellent stability up to 160 °C. The practical benefits of this synergistic strategy are exhibited in force-electric energy conversion applications. The multilayer ceramic capacitors (MLCC-BNT) deliver a record-breaking peak pulse current of 90 A via a pressure-induced phase transition from the ferroelectric *R*3*c* phase to the nonpolar *Pnma* phase. The proposed strategy provides a highly feasible approach for enhancing the ferroelectricity and thermal stability of lead-free ferroelectric materials, thereby establishing a solid material foundation for high-power force-electric energy conversion.

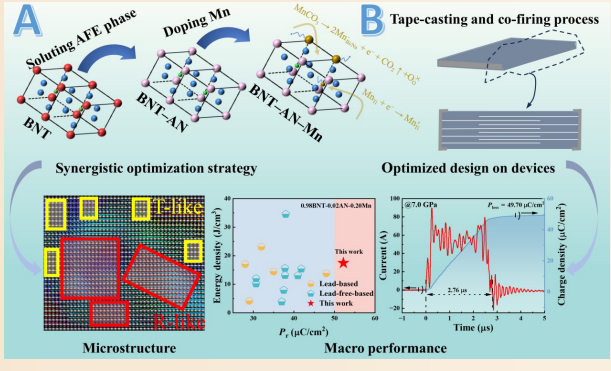

KEYWORDS: bismuth sodium titanate; ultrahigh remanent polarization; thermal stability of remanent polarization; structural distortions; defect engineering; force-electric energy conversion

1 Introduction

The ever-increasing global demand for energy has driven intense research interest in the area of energy harvesting and conversion, encompassing energy storage devices such as electrochemical batteries, thermal batteries, and electrochemical capacitors [1]. Among them, high-power force-electric energy conversion systems are particularly attractive for applications requiring long storage lifetimes, ultrafast responses, and high current or voltage outputs, which are difficult to achieve using conventional electrochemical batteries, thermal batteries, or supercapacitors [2]. These high-power force-electric energy conversion systems utilize the pressure-induced polar–nonpolar phase transition of ferroelectric ceramic materials under shock compression to instantaneously deliver megawatt-level high-power pulsed current/voltage [3,4]. In such a system, the remanent polarization

[1] School of Chemistry and Materials Science, Hangzhou Institute for Advanced Study, University of Chinese Academy of Sciences, Hangzhou 310024, China. [2] The State Key Laboratory of High Performance Ceramics, and Superfine Microstructure, Shanghai Institute of Ceramics, Chinese Academy of Sciences, Shanghai 201899, China. [3] Joint Laboratory for Extreme Conditions Matter Properties, School of Mathematics and Physics, Southwest University of Science and Technology, Mianyang 621010, China. [4] Center for High Pressure Science and Technology Advanced Research (HPSTAR), Shanghai 201203, China. [5] Institute of Fluid Physics, China Academy of Engineering Physics, Mianyang 621900, China. [6] Center of Materials Science and Optoelectronics Engineering, University of Chinese Academy of Sciences, Beijing 100049, China.

✉ Corresponding authors. E-mail: M. Xie, xiemeng@mail.sic.ac.cn; H. Nie, sestonenhc@mail.sic.ac.cn; G. Wang, genshuiwang@mail.sic.ac.cn

Received: April 2, 2026; Revised: May 28, 2026; Accepted: July 5, 2026

(P_r) is a key parameter because the theoretical energy density (w) of ferroelectric materials can be expressed as $w = P_r^2/(2\varepsilon_r\varepsilon_0)$ [2], where ε_r and ε_0 represent the relative permittivity after pressure-driven depolarization and permittivity of free space, respectively. This relationship indicates that a large P_r is essential for achieving high energy output. Moreover, since these devices often operate under elevated-temperature conditions, the thermal stability of P_r is equally critical for maintaining reliable performance. On the other hand, bulk ferroelectric ceramics and single crystals are constrained by their limited electrode area, resulting in an insufficient release of bound charges and making it difficult to generate substantial electrical energy [5]. Consequently, practical applications often require parallel connected structures to achieve high energy output, which hinders miniaturization and integration. Therefore, developing ferroelectric materials that simultaneously possess high remanent polarization and excellent thermal stability, as well as achieving optimized design on ferroelectric devices, are of both scientific and technological importance for high-power force-electric energy conversion.

To date, lead-based ferroelectric ceramics have dominated high-power force-electric energy conversion applications. Among them, a representative system is ~2% Nb-doped lead zirconate titanate ($Pb_{0.99}(Zr_{0.95}Ti_{0.05})_{0.98}Nb_{0.02}O_3$), which can release bound charges, achieving high energy output via a pressure-driven ferroelectric–antiferroelectric (FE–AFE) phase transition and has dominated the commercial market for more than half a century [6]. However, increasingly stringent environmental regulations and the demand for lightweighting have motivated the development of lead-free alternatives. Among various lead-free candidates, bismuth sodium titanate ($Bi_{0.5}Na_{0.5}TiO_3$) [7–14], silver niobate ($AgNbO_3$) [15–17], sodium niobate ($NaNbO_3$) [18], and sodium bismuth titanate ($Bi_{0.5}Na_{0.5}TiO_3$ (BNT))-based ceramics have emerged as promising candidates owing to their abundant phase structure and outstanding ferroelectric performance [7–14]. Driven by an external electric field, the internal nanodomains in BNT undergo continuous rotation and high-degree alignment, allowing them to retain a relatively high remanent polarization after the removal of the electric field [7]. In recent years, considerable efforts have been devoted to enhancing the ferroelectric performance of BNT-based ceramics through multicomponent solid solution strategies. For example, Peng *et al.* [8,9] introduced $BiAlO_3$ (BA) and $NaNbO_3$ (NN) into BNT-based ceramics, achieving a remanent polarization of 36.5 μC/cm^2 by inducing the coupling and growth of polar nanoregions (PNRs) into macroscopic ferroelectric domains. Similarly, in a ternary BNT-based system constructed by introducing BA and $K_{0.5}Na_{0.5}NbO_3$ (KNN), Liu *et al.* [12] effectively tuned the phase boundary to render the material in a highly sensitive metastable ferroelectric phase, thereby obtaining a remanent polarization of 32.3 μC/cm^2. These studies have demonstrated that multicomponent solid solution strategies can effectively enhance the polarization response. Although the multicomponent solid solution strategy can effectively enhance the ferroelectric properties of BNT-based ceramics, it typically reduces their depolarization temperature to approximately 100 °C. More critically, the volatilization of Bi/Na during high-temperature sintering leads to the formation of oxygen vacancies and the reduction of Ti^{4+}, which not only increases the leakage current but also compromises the thermal stability of the ceramics [10]. These results indicate that it remains highly challenging to simultaneously achieve high remanent polarization and excellent thermal stability in BNT-based ferroelectrics through a single multicomponent solid solution strategy.

Defect engineering has been widely recognized as an effective strategy to suppress the leakage current density and enhance the thermal stability of ceramic materials, an effect primarily attributed to the formation of dopant-vacancy defect complexes or defect dipoles. For instance, in $(Ba_{0.5}Sr_{0.5})TiO_3$-based ceramics, doped MnO_2 combines with oxygen vacancies to form defect complexes, which effectively block conduction pathways through charge compensation, thereby significantly suppressing the leakage current density [19]. Furthermore, defect dipoles can strongly couple with ferroelectric domains to induce a domain wall pinning effect and inhibit thermally induced domain destabilization; benefiting from this, $(Li_{0.5}Bi_{0.5})_{0.40}Bi_2Nb_2O_9$ (CBNL)-based ceramics exhibit excellent thermal stability, retaining 92% of their initial d_{33} value after annealing at 800 °C [20]. Similarly, the construction of defect dipoles can also induce and intensify local oxygen octahedral distortion, thereby effectively enhancing domain activity and substantially increasing the d_{33} value of $CaBi_4Ti_4O_{15}$-based ceramics by 50% [21]. From this perspective, defect engineering is expected to address the long-standing challenge of insufficient thermal stability in BNT-based ferroelectric materials. In addition to intrinsic structure optimization, practical high-power force-electric energy conversion also places stringent requirements on device architecture. Relying on their unique laminated architecture, multilayer ceramic capacitors (MLCCs) have effectively broken through the performance bottlenecks of traditional bulk ceramics, demonstrating outstanding performance-enhancing advantages in dielectric energy storage applications. Specifically, in $BaTiO_3$-based ceramics, the introduction of the MLCC structure not only broadens the thermal stability of the material over a wide temperature range but also enables a high energy storage density of 6.09 J/cm^3 [22]. Furthermore, the multilayer design of MLCCs endows lead-free energy-storage ceramics with an extremely low equivalent series resistance, providing them with significant advantages in high-power-density electronic systems [23]. Similarly, by introducing ultrathin dielectric layers, the MLCC architecture significantly improves the breakdown strength and voltage-withstanding capability of ceramic materials, thereby substantially enhancing the overall discharge energy density [24]. These studies indicate that the MLCC architecture can not only efficiently translate excellent intrinsic material properties into robust pulse-output performance but also strongly promote the miniaturization and integration of devices.

Based on the above considerations, we propose a synergistic optimization strategy that integrates composition-driven structural distortion, defect-engineering-induced pinning effects, and multilayer device architecture to simultaneously enhance the remanent polarization, thermal stability, and practical output performance of lead-free ferroelectric ceramics. Specifically, antiferroelectric silver niobate (AN) is introduced into BNT to intensify lattice distortion and construct a polymorphic nanodomain structure, thereby lowering the domain-switching energy barrier and favoring a larger remanent polarization. Based on the previous research of our group [7], $0.98Bi_{0.5}Na_{0.5}TiO_3$–$0.02AgNbO_3$ was selected as the matrix material in this study. Subsequently, an appropriate amount of $MnCO_3$ is introduced to couple with A-site vacancies and form defect complexes, which act as strong pinning centers to suppress thermally induced ferroelectric domain switching and improve the thermal stability of P_r. Furthermore, a tape-casting co-firing process is employed to fabricate multilayer ceramic capacitors to significantly enhance the output capability. As a result of this synergistic strategy, the lead-free 0.98BNT–0.02AN–0.20 wt%

$MnCO_3$ ceramics exhibit an ultrahigh remanent polarization of 52.21 μC/cm^2, together with excellent thermal stability up to 160 °C. High-angle annular dark-field scanning transmission electron microscopy (HAADF-STEM) observations confirm the formation of a polymorphic nanodomain structure, which is beneficial for reducing the domain-switching energy barrier and enhancing the polarization response. Meanwhile, the defect complexes formed in the system effectively stabilize the ferroelectric domains against thermal perturbation. *In situ* Raman spectroscopy reveals that the material undergoes a complete depolarization phase transition from the polar *R3c* phase to the nonpolar *Pnma* phase under dynamic shock compression. More importantly, the fabricated multilayer ceramic capacitors (MLCC-BNT) show excellent ferroelectricity and thermal stability, releasing a record-breaking peak pulse current of 90 A. These results demonstrate that the proposed synergistic strategy is highly effective for simultaneously enhancing ferroelectricity and thermal stability in lead-free ferroelectric materials and thus establishes a solid material foundation for high-performance, high-power force-electric energy conversion.

2 Experimental

2.1 Sample synthesis

Ceramic preparation: The $0.98Bi_{0.5}Na_{0.5}TiO_3$–$0.02AgNbO_3$–$x$ wt% $MnCO_3$ (x = 0, 0.05, 0.10, 0.15, 0.20, and 0.25) ceramics were synthesized through a conventional solid-state reaction method. The raw materials, including Bi_2O_3 (99.9%), Na_2CO_3 (99.8%), TiO_2 (99.5%), Ag_2O (99.95%), Nb_2O_5 (99.5%), and $MnCO_3$ (99.99%), were first dried at 100 °C for 10 h. Subsequently, the powders were weighed according to the stoichiometric composition and then planetary ball-milled with ethanol for 6 h. The ball-to-powder ratio was fixed at 2: 1, and the rotational speed was maintained at 400 r/min. After drying at 75 °C, the milled powders were calcined at 850 °C for 3 h with a ramp rate of 2 °C/min. The calcined powders were remilled and dried under the same conditions. Next, 7 wt% polyvinyl alcohol (PVA) was added as a binder. The powders, with the aid of PVA, were pressed into pellets with a thickness of 1.5 mm and a diameter of 13 mm. Subsequently, the pellets were heated to 650 °C for 3 h to remove the binder. To minimize the volatilization of Bi and Na, the pellets were buried in powders of the same composition and then sintered at 1160–1200 °C for 2 h with a ramp rate of 2 °C/min.

MLCCs fabrication: The same powder synthesized for ceramic preparation was placed in an attrition mill with zirconia balls as the milling media. The powder was finely milled at 500 r/min for 4 h with a mass ratio of powder to milling media to anhydrous ethanol of 1 : 10 : 2. Subsequently, the finely milled ceramic powder (40 wt% of the slurry), a mixed solvent of anhydrous ethanol and ethyl acetate (53.9 wt% of the slurry), and a dispersant (AKM0531; 0.3 wt% of the slurry) were mixed via ball milling for 4 h. Next, a binder (polyvinyl butyral; 4.0 wt% of the slurry) and a plasticizer (dioctyl phthalate; 1.8 wt% of the slurry) were added, followed by continuous ball milling for 24 h to obtain the ceramic slurry. After vacuum degassing, the slurry was tape-cast into green tape, followed by the screen printing of Ag/Pd (70/30) internal electrodes. Blank and electrode-printed tapes were stacked layer by layer according to the MLCC design specifications. The stacked layers were isostatically laminated at 70 °C and 64 MPa for 20 min and then cut into individual blocks. The blocks were heated to 330 °C and held for 5 h to remove the organic binders, yielding multilayer ceramic green bodies. They were then sintered at 1080 °C for 2 h with a heating rate of 2 °C/min to form the final MLCC-BNT. The sintered dielectric layer thickness was approximately 40 μm.

2.2 Material characterizations

The crystal structure was analyzed using an X-ray diffractometer (XRD; D/MAX-2550V, Rigaku, Japan). Rietveld refinement of the full patterns was performed using GSAS to obtain specific cell parameters and phase fractions. Raman spectra were collected using a Raman spectrometer (inVia Reflex, Renishaw, UK). The microstructure was observed by a scanning electron microscope (SEM; SU3500, Hitachi, Japan) and a transmission electron microscope (TEM; JEM-F200, JEOL, Japan). The chemical elemental composition of the samples was analyzed using an inductively coupled plasma-optical emission spectrometer (ICP-OES; Agilent 5110, USA). The chemical valence state was identified by an X-ray photoelectron spectrometer (XPS; ESCALAB Xi, USA). The electron spin resonance (EPR) experiments were carried out with an EPR spectrometer (JES-FA200, JEOL, Japan) at X-band frequencies of 9.1 GHz at room temperature with a microwave power of 1 mW. Local atomic-scale structures were investigated using a Cs-corrected high-angle annular dark-field scanning transmission electron microscope (FEI spectra 300, Thermo Scientific, USA).

2.3 Electrical property measurements

For electrical testing of the bulk ceramics, the bulk ceramics were polished on both sides to a thickness of 0.5 mm. Subsequently, Ag electrodes with a diameter of 8 mm were screen-printed on both surfaces and fired at 650 °C for 0.5 h with a ramp rate of 2 °C/min. For the MLCCs, the single-layer effective electrode dimensions were 7.21 mm × 6.96 mm; with 7 active dielectric layers, the total effective electrode area was 351.27 mm^2. The temperature-dependent dielectric properties were evaluated by a precision inductance capacitance resistance (LCR) meter (E4980A, Agilent, USA). The polarization–electric (P–E) loops were recorded using a ferroelectric measurement system (TF Analyzer 2000E, aixACCT Co., Germany) by applying a triangular waveform electrical signal at frequencies of 1–150 Hz under electric fields of 4–8 kV/mm. Prior to the depolarization tests, the samples were pre-poled in a silicone oil bath at room temperature under a direct current (DC) electric field of 8 kV/mm for 20 min. The piezoelectric coefficient d_{33} was then measured using a quasi-static d_{33} meter (ZJ-7A, Institute of Acoustics, Chinese Academy of Sciences, China). The remanent polarization (P_r) after poling was quantitatively evaluated using a lab-assembled rapid high-temperature depolarization (HTD) device: The poled samples were placed in silicone oil at 250 °C, and the released charges were collected and integrated using an electrometer connected with a standard capacitor. Hydrostatic–pressure depolarization tests were conducted in a lab-assembled hydrostatic pressure loading system at room temperature using silicone oil as the pressure-transmitting medium. The pressure was continuously loaded at a rate of 10 MPa/s up to 600 MPa, and the released charges were similarly measured via an external standard capacitor and an electrometer. The dynamic shock compression experiments were carried out in a perpendicular mode (with the polarization direction perpendicular to the shock wave propagation direction) using a one-stage light-gas gun facility, where the shock waves were generated by the impact of copper flyers on the sample. During the charge release process induced by shock-driven phase transition depolarization, the discharge signals were captured and recorded using a picosecond oscilloscope.

3 Results and discussion

The 0.98BNT–0.02AN–x wt% $MnCO_3$ (BNT–AN–Mn) ceramics have a dense microstructure with grain sizes varying from 1 to 1.8 μm and relative densities between 97.1% and 97.7% (Fig. S1 in the Electronic Supplementary Material (ESM)). As shown in Fig. 1(a), the P–E hysteresis loops of the BNT–AN–Mn ceramics were measured at room temperature. All compositions display typical single-loop-featured FE characteristics. When x = 0.20, the material exhibits the highest remanent polarization (P_r) of approximately 52.21 μC/cm^2; however, as x increases to 0.25, the P_r decreases. This suggests that the appropriate addition of Mn facilitates the formation of ferroelectric domains, thereby enhancing ferroelectricity [25]. The leakage current density of the ceramics with different $MnCO_3$ contents is shown in Fig. 1(b). The leakage current density decreases with increasing x, and the minimum value is obtained at x = 0.20. As a direct method to assess energy storage performance for force-electric conversion applications, P_r was calculated via rapid high-temperature depolarization (HTD) tests by collecting the depolarization charges [7]. As shown in Fig. 1(c) and Table S1 in the ESM, the variation trend of the values obtained from the depolarization tests is consistent with the trend calculated from the P–E loops.

The thermal stability of ferroelectric materials is also a critical factor for material selection and device design [15]. From Fig. 1(d) and Fig. S2 in the ESM, it is found that as the Mn content increases, the rate of change of the remanent polarization first decreases and then increases, being minimal at x = 0.20, indicating that this composition possesses the highest thermal stability of its ferroelectricity. Figure 1(e) and Fig. S3 in the ESM show the dielectric constant of the ceramics as a function of temperature from 25 to 450 °C. No obvious abrupt change in the dielectric constant is observed below 160 °C. Figure S4 in the ESM shows the thermally stimulated depolarization current curves of 0.98BNT–0.02AN–0.20 wt% $MnCO_3$ ceramics from 30 to 300 °C. A sharp depolarization peak does not appear until the temperature reaches approximately 160 °C, which can be attributed to the ferroelectric–relaxor ferroelectric (FE–RFE) phase transition [26], further supporting the excellent thermal stability of the 0.98BNT–0.02AN–0.20 wt% $MnCO_3$ ceramics. Figure 1(g) compares the P_r and T_d of various BNT ferroelectric materials [7–14]. The P_r and thermal stability of the 0.98BNT–0.02AN–0.20 wt% $MnCO_3$ ferroelectric ceramic are at a leading level among existing BNT ferroelectric materials used for high-power force–electric energy conversion applications. Furthermore, as illustrated in Fig. S5 in the ESM, the 0.98BNT–0.02AN–0.20 wt% $MnCO_3$ ferroelectric ceramic

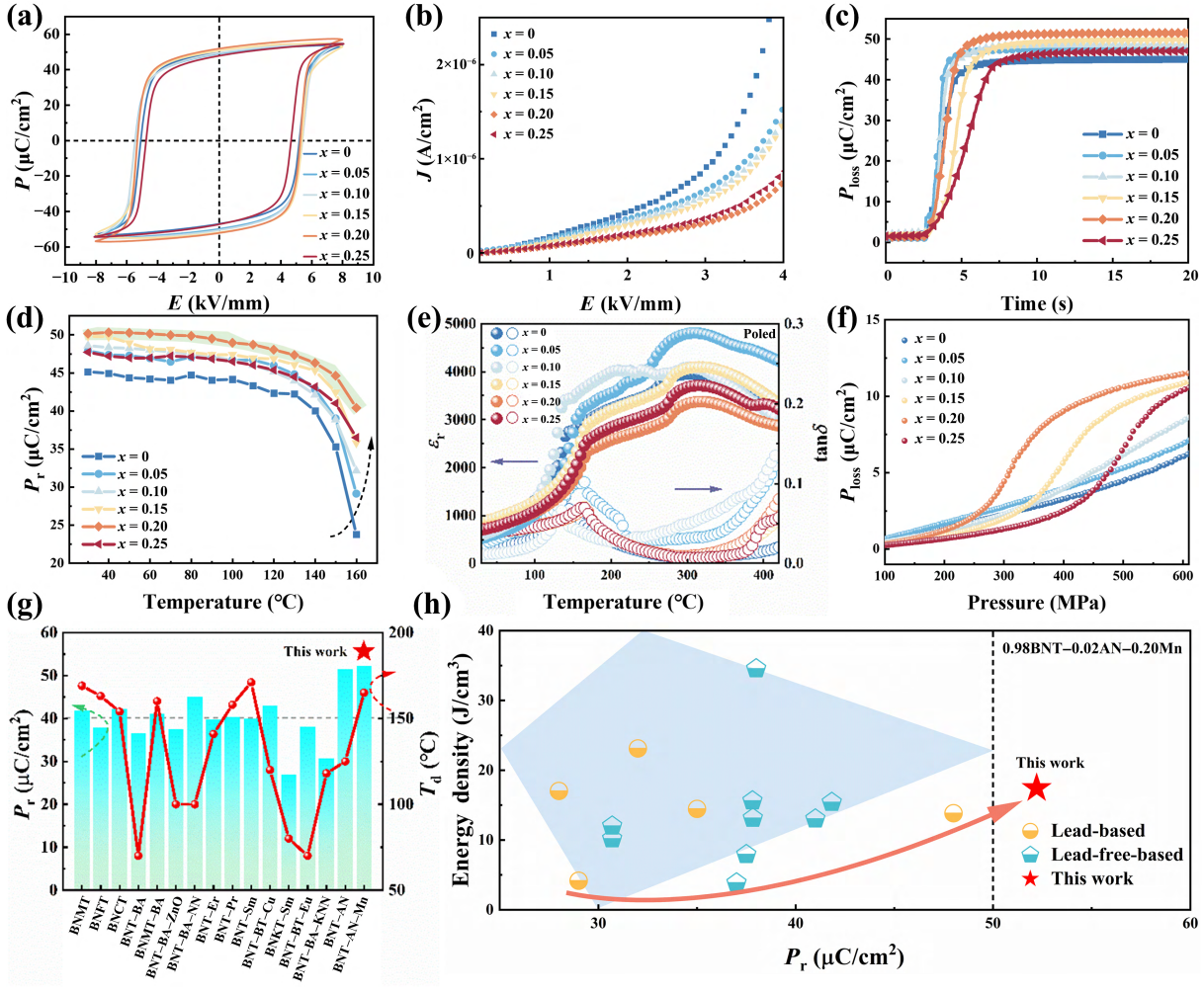

Fig. 1 Macroscopic performance of 0.98BNT–0.02AN–x wt% $MnCO_3$ ceramics: (a) P–E loops, (b) leakage current curves, and (c) thermal depolarization curves. (d) Temperature-dependent P_r curves, (e) temperature-dependent dielectric properties, and (f) *in situ* depolarization curves under hydrostatic pressures of poled 0.98BNT0.02AN–x wt% $MnCO_3$ ceramics. (g) Summary of P_r and T_d for BNT-based ceramics. (h) Comparison of performance of FE materials for force-electric energy conversion.

exhibits excellent frequency stability in the frequency range from 1 to 150 Hz, maintaining reliable ferroelectric performance.

To evaluate their *in situ* depolarization behavior under pressure, the poled samples were placed in an oil hydrostatic pressure environment at room temperature. Figure 1(f) shows the *in situ* depolarization curve of the BNT–AN–Mn ceramics with increasing hydrostatic pressure at room temperature. Unlike PZT 95/5 ceramics [27], BNT–AN–Mn ceramics do not exhibit a distinct critical depolarization pressure under the tested isostatic conditions. Under 600 MPa hydrostatic pressure, the sample with x = 0.20 releases the maximum polarization of approximately 12.13 μC/cm^2, demonstrating excellent force–electric energy conversion ability [28]. The theoretical energy density (w) of FE materials can be calculated using equation $w = P_r^2/(2\varepsilon\varepsilon_0)$ [2], where ε and ε_0 represent the relative permittivity after pressure-driven depolarization and permittivity of free space, respectively This equation provides an idealized baseline for comparing intrinsic material properties. In practical force-electric conversion systems, the actual releasable electrical output is more complex and depends strongly on dynamic discharge characteristics, depolarization kinetics, and external circuit conditions. Nevertheless, this fundamental relationship dictates that a large P_r is an essential prerequisite for achieving high power energy output. Figure 1(h) compares the theoretical energy densities of various ferroelectric materials [5,14–35]. The 0.98BNT–0.02AN–0.20 wt% $MnCO_3$ ferroelectric ceramics achieve energy storage density of 19.52 J/cm^3, which is significantly higher than that of most ferroelectric materials. These results indicate that the 0.98BNT–0.02AN–0.20 wt% $MnCO_3$ ferroelectric ceramics have great potential for high-power force-electric energy conversion applications. Furthermore, this work conducted an investigation into the structural origin of the excellent performance of 0.98BNT–0.02AN–0.20 wt% $MnCO_3$ ceramics and their phase transition behavior under external fields, which is of great significance for enhancing the understanding of the performance enhancement mechanism of ferroelectric materials.

Figure 2(a) displays the XRD patterns of the 0.98BNT–0.02AN–x wt% $MnCO_3$ ceramics, revealing that all compositions possess a pure perovskite structure [35]. As evidenced by Fig. 2(b) and Fig. S6 in the ESM, the Rietveld refinement results based on a dual-phase model (*R3c* and *Pm3m*) indicate a monotonic increase in the *R3c* phase content and the *c*/*a* ratio. This suggests that the introduction of $MnCO_3$ increases the content of the ferroelectric rhombohedral phase and induces lattice distortion, which contributes to the stabilization of the ferroelectric phase and is beneficial for enhancing the P_r and thermal stability [36]. The *Pm3m* phase applied in the Rietveld model represents an average crystallographic symmetry over a macroscopic scale. In BNT-

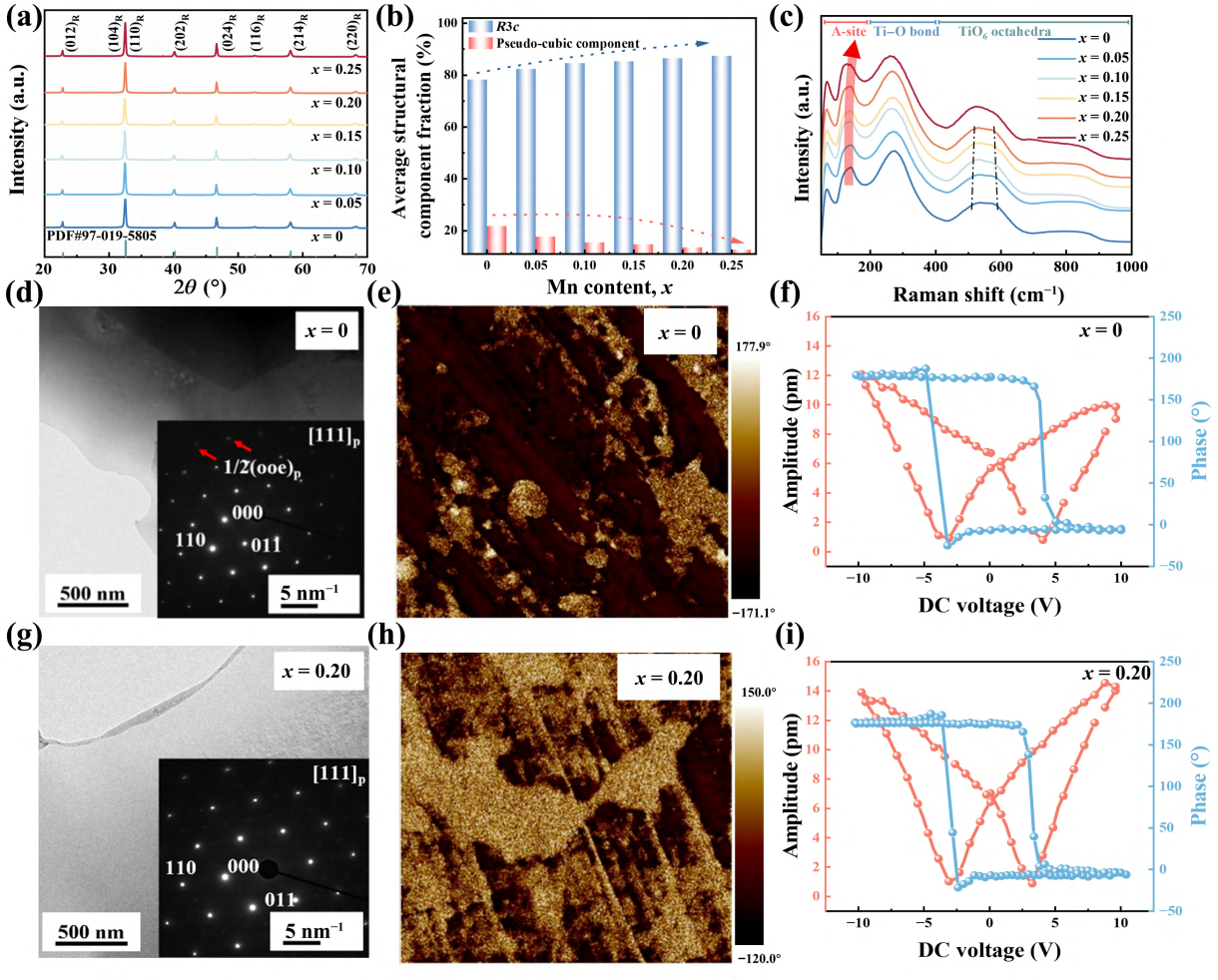

Fig. 2 Structural analysis of 0.98BNT–0.02AN–x wt% $MnCO_3$ ceramics: (a) XRD patterns, (b) variation trend of phase contents, and (c) Raman spectra of 0.98BNT–0.02AN–x wt% $MnCO_3$ ceramics. TEM images taken along $[111]_p$ zone axis directions of 0.98BNT–0.02AN–x wt% $MnCO_3$ ceramics: (d) x = 0 and (g) x = 0.20. Insets show corresponding SAED patterns. PFM phase images of 0.98BNT–0.02AN–x wt% $MnCO_3$ ceramics: (e) x = 0 and (h) x = 0.20. Local PFM amplitude butterfly curves and phase hysteresis loops of 0.98BNT–0.02AN–x wt% $MnCO_3$ ceramics: (f) x = 0 and (i) x = 0.20.

based relaxor systems, such a macroscopically pseudo-cubic phase typically originates from the spatial average of highly localized, structurally distorted nanoregions (e.g., tetragonal domains) that cannot be fully resolved by standard XRD due to its limited coherence length. Raman spectroscopy was employed to further investigate the stabilizing effect of $MnCO_3$ on the ferroelectric phase. With increasing Mn content, the peaks near 180 and 260 cm^{-1} shift toward higher wavenumbers. This indicates that as x increases, the bond energy is strengthened and the lattice contracts, driving the phase transition toward the rhombohedral phase [37,38].

To further explore the intrinsic relationship between macroscopic properties and the microscopic structure, high-resolution TEM (HRTEM) images of the x = 0 and 0.20 compositions taken along the $[110]_p$ and $[111]_p$ zone axes are shown in Figs. 2(d) and 2(g) and Fig. S7 in the ESM, with the corresponding selected-area electron diffraction (SAED) patterns displayed in the insets. The SAED patterns along the $[110]_p$ and $[111]_p$ zone axes show clear 1/2(ooo) and weak 1/2(ooe) superlattice reflections ("o" and "e" refer to odd and even *hkl* indices, respectively) (red arrows in Fig. 2(d) and orange arrows in Fig. S7 in the ESM) [39]. The 1/2(ooo) reflection spots indicate the presence of polar *R3c* symmetry with an anti-phase $a^-a^-a^-$ oxygen octahedron tilt, while the 1/2(ooe) reflection spots correspond to in-phase $a^0b^+a^-$ oxygen octahedral tilting [40]. The existence of 1/2(ooe) reflection spots confirms the presence of non-*R3c* phases, which is in agreement with the aforementioned result of average *Pm3m* symmetry observed in macroscopic XRD patterns. As shown in Figs. 2(d) and 2(g), both 1/2(ooo) and 1/2(ooe) superlattice reflections are present at x = 0, indicating the coexistence of the *R3c* and non-*R3c* phases in the crystal structure. In contrast, for the x = 0.20 composition, the 1/2(ooe) superlattice reflection is not observed, suggesting that the *R3c* phase is enhanced. This is consistent with the XRD refinement results, further confirming the stabilizing effect of Mn on the ferroelectric phase. Piezoresponse force microscopy (PFM) was performed to study the influence of Mn on the ferroelectric domain structure. Figures 2(e) and 2(h) display the PFM amplitude images for the x = 0 and 0.20 compositions under identical testing conditions, respectively. From the contrast of the amplitude images, for the x = 0.20 composition, the ferroelectric domain boundaries are more distinct and the domain size is relatively larger than that for the x = 0 composition, which suggests that the enhancement of macroscopic ferroelectric properties may be related to the growth of ferroelectric domains [41]. Furthermore, as illustrated in Figs. 2(f) and 2(i), compared with the undoped sample, the 0.98BNT–0.02AN–0.20 wt% $MnCO_3$ ceramic exhibits a higher maximum piezoelectric amplitude, a lower coercive voltage, and sharper phase switching, indicating a lower domain switching energy barrier and more enhanced ferroelectricity.

Figures 3(a)–3(c) and Fig. S8 in the ESM display the temperature-dependent evolution of the *P*–*E* and *I*–*E* loops for the 0.98BNT–0.02AN–x wt% $MnCO_3$ ceramics from 30 to 160 °C. In contrast to the other samples, the x = 0.20 ceramic maintains typical ferroelectric *P*–*E* loops with higher P_r values at a high temperature, indicating the excellent thermal stability of ferroelectricity. Meanwhile, four current peaks are observed at approximately 100 °C for x = 0, indicating the occurrence of an FE–RFE phase transition [37], whereas no distinct four current peaks appear for x = 0.20 up to 150 °C, further confirming the superior thermal stability of this composition.

To investigate the structural origin of the thermal stability of 0.98BNT–0.02AN–0.20 wt% $MnCO_3$ ceramics, temperature-dependent XRD patterns and Raman spectroscopy were performed on the ceramics. As shown in Fig. 3(d), in the temperature range from 30 to 450 °C, all XRD peaks shift toward lower angles with increasing temperature, which can be attributed to the unit cell volume expansion caused by elevated temperatures [42]. Additionally, a distinct discontinuity and abrupt change in the red band near 46.5° is observed for x = 0. The peak position and width change abruptly, whereas for x = 0.20, the red band exhibits a continuous and smooth leftward shift throughout the heating process without any obvious discontinuity. This indicates that the defect engineering triggered by the introduction of Mn suppresses the thermally induced structural abrupt transition, transforming it into a diffuse phase transition. This structural feature implies that the 0.98BNT–0.02AN–0.20 wt% $MnCO_3$ ceramic can still maintain robust ferroelectricity at high temperatures without undergoing sudden depolarization. Concurrently, as shown in Fig. 3(e) and Fig. S9 in the ESM, the number of Raman peaks remains almost unchanged in the temperature range from 30 to 210 °C, suggesting that the overall structure is stable over a wide temperature range [43]. However, with increasing temperature, all peaks exhibit pronounced broadening and smoothing, which correlates with reduced unit cell polarity caused by intensified thermal agitation [44]. For the (TO_3) mode at 500–600 cm^{-1}, the two peaks shift toward higher and lower wavenumbers, respectively, and the intensity of the left peak gradually increases, while that of the right peak decreases. This variation can be attributed to the FE–RFE phase transition [37]. As shown in Fig. 3(f), the wavenumber variations of the various modes are relatively gradual without drastic jumps, further corroborating the structural stability during the heating process. This remarkable thermal stability is attributed to the pinning effect resulting from the defect engineering introduced by Mn, which effectively suppresses the abrupt structural transition [44].

To determine the actual chemical composition of the 0.98BNT–0.02AN–x wt% $MnCO_3$ ceramics and to verify whether Mn was successfully incorporated into the matrix, we conducted an ICP-OES analysis. As shown in Tables S4 and S5 in the ESM, the actual chemical formulas reveal a slight deficiency in Bi and Na compared with the theoretical composition, indicating that the volatilization of Bi and Na occurred during the high-temperature sintering process. Furthermore, the variation trend of the elemental molar ratios (Fig. S10 in the ESM) shows that the actual Mn content increases proportionately with increasing x. This indicates that the Mn additive has been successfully incorporated into the matrix, without obvious segregation or compositional deviation.

To better elucidate the mechanism of action of defect engineering on the ferroelectric properties of ceramics, EPR and XPS measurements were performed on 0.98BNT–0.02AN–x wt% $MnCO_3$ ceramics. Mn ions exist in multiple valence states [45]. The upper part of Fig. 4(a) shows the EPR spectrum of the undoped ceramic, where a weak paramagnetic resonance absorption peak is detected at approximately 322 mT. Since there are no magnetic ions in the undoped ceramic system, this weak signal should originate from oxygen vacancies, verifying that some oxygen vacancy defects exist in the undoped ceramics. However, in the EPR spectrum of the 0.98BNT–0.02AN–0.20 wt% $MnCO_3$ ceramic, two paramagnetic resonance absorption peaks are observed, as shown in the lower part of Fig. 4(a). One is a broad peak near 325 mT with a *g*-factor of 1.97, which is very close to the *g*-factor of free electrons (g_e = 2.0023) [46], indicating that the 3d orbital of Mn is half-filled ($3d^5$) and that the Mn ions exist in the form of Mn^{2+} [47]. The other is a weak peak near 172 mT with

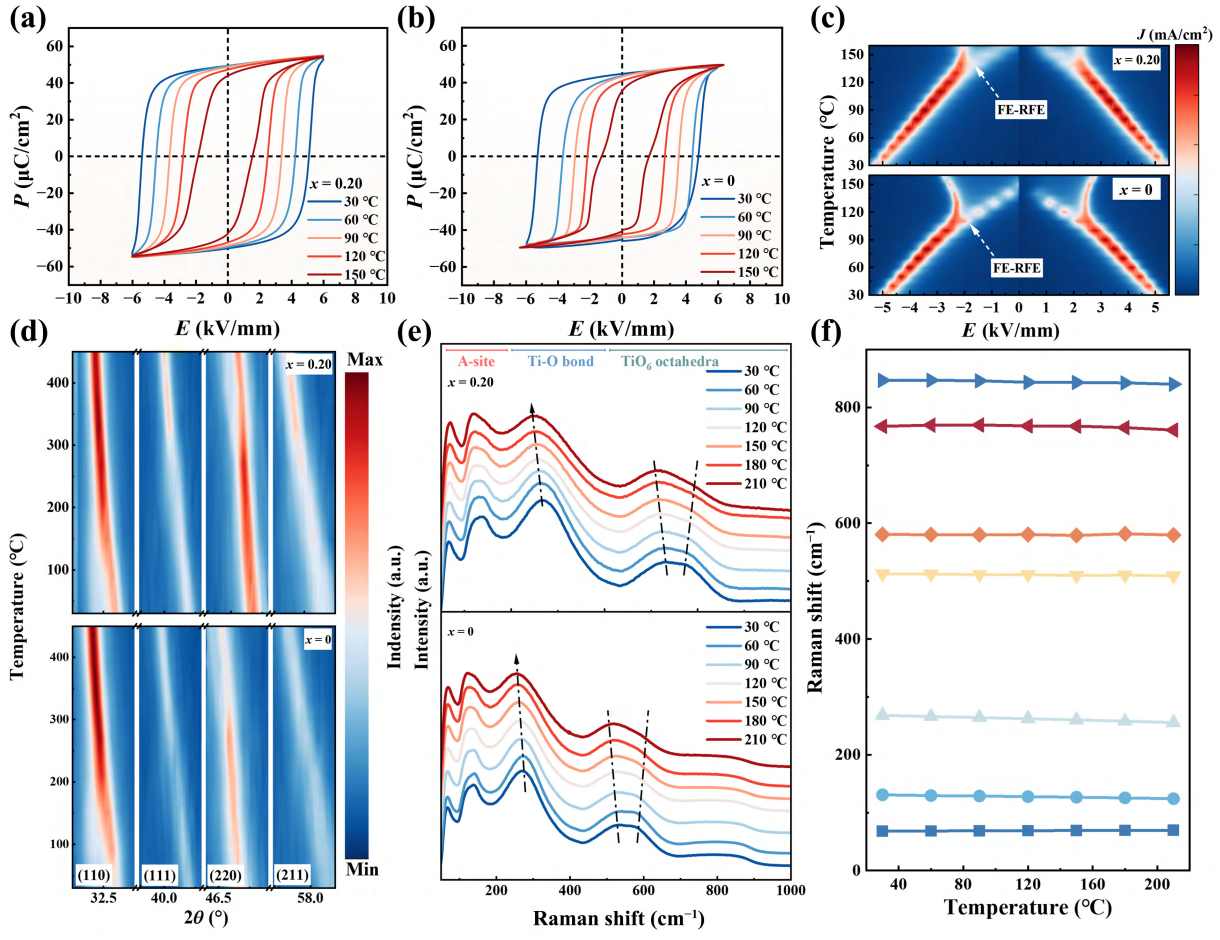

Fig. 3 Thermal stability analysis of 0.98BNT–0.02AN–*x* wt% $MnCO_3$ ceramics: Temperature-dependent *P*–*E* loops of (a) 0.98BNT–0.02AN–0.20 wt% $MnCO_3$ and (b) 0.98BNT–0.02AN ceramics. (c) Temperature-dependent *I*–*E* loops of 0.98BNT–0.02AN and 0.98BNT–0.02AN–0.20 wt% $MnCO_3$ ceramics. (d) Temperature-dependent XRD patterns and (e) temperature-dependent Raman spectra of 0.98BNT–0.02AN and 0.98BNT–0.02AN–0.20 wt% $MnCO_3$ ceramics. (f) Temperature-dependent evolution of deconvoluted Raman peaks of 0.98BNT–0.02AN–0.20 wt% $MnCO_3$ ceramics.

a *g*-factor of 3.79, corresponding to Mn^{4+} ions [46]. These results indicate that Mn ions have been successfully incorporated into the crystal lattice, coexisting as Mn^{2+} and Mn^{4+}.

To more clearly illustrate the suppressive effect of defect engineering on the reduction process of Ti^{4+}, Fig. 4(d) provides a schematic diagram of the lattice defect. In the undoped sample, high-temperature sintering leads to the volatilization of A-site Bi^{3+} and Na^+ ions. To achieve charge compensation, A-site vacancies and oxygen vacancies are simultaneously generated in the system [48]. When lattice oxygen escapes in the form of O_2, it releases free electrons (e'). These electrons are highly susceptible to being captured by B-site Ti^{4+}, reducing it to Ti^{3+}, which subsequently forms an n-type electronic conduction channel and significantly increases the leakage current [21]. However, in the 0.98BNT–0.02AN–0.20 wt% $MnCO_3$ ceramics, high-valence Mn ions entering the B-site act as effective "electron traps". They preferentially capture the free electrons in the system, effectively blocking the transfer of electrons to Ti^{4+} and suppressing the reduction of Ti^{4+} to Ti^{3+}. To verify this mechanism, Fig. 4(b) compares the high-resolution XPS spectra of Ti $2p_{1/2}$ and Ti $2p_{3/2}$ in 0.98BNT–0.02AN and 0.98BNT–0.02AN–0.20 wt% $MnCO_3$. As *x* varies from 0 to 0.20, the Ti^{3+} concentration decreases from approximately 4.15% to 3.17%, corroborating that defect engineering can indeed inhibit the reduction of Ti ions [49]. Furthermore, the bandgap values of the ceramics were calculated based on the Kubelka–Munk theory, revealing that a maximum value of 3.19 eV is obtained at $x = 0.20$, as shown in Fig. 4(c). This indicates that the defect dipoles induced by an appropriate amount of Mn doping can increase the barrier height for electron transition from the valence band to the conduction band, thereby effectively suppressing the generation and migration of charge carriers and consequently reducing the leakage current density and dielectric loss [50]. In addition, the improvement in ferroelectric properties may also be related to the reduction in dielectric loss [51]. Domain wall vibration is a significant source of loss in ferroelectrics [51]. Numerous studies have reported that Mn doping leads to the formation of defect dipoles [41]. Therefore, it is suggested that the introduction of Mn can hinder domain wall vibration, which is conducive to enhancing ferroelectricity. As shown in Fig. S11 in the ESM, the loss of the unpoled ceramic reaches a minimum at $x = 0.20$. However, excessive Mn doping may induce an increase in defects, leading to a significant increase in the dielectric loss for the $x = 0.25$ composition, thereby suppressing the ferroelectric properties.

To further investigate the intrinsic physical origins of the ultrahigh remanent polarization (P_r = 52.21 μC/cm²) and excellent thermal stability up to 160 °C in the 0.98BNT–0.02AN–0.20 wt% $MnCO_3$ ceramics, spherical aberration-corrected HAADF-STEM was utilized to characterize their nanoscale atomic arrangement, local chemical environment, and domain structure [52]. The local polarization vector of each unit cell, determined by the displacement of the A-site cation relative to the geometric center of adjacent B-site cations, is represented by arrows of different colors and lengths in Fig. 5(d). The variations in the magnitude

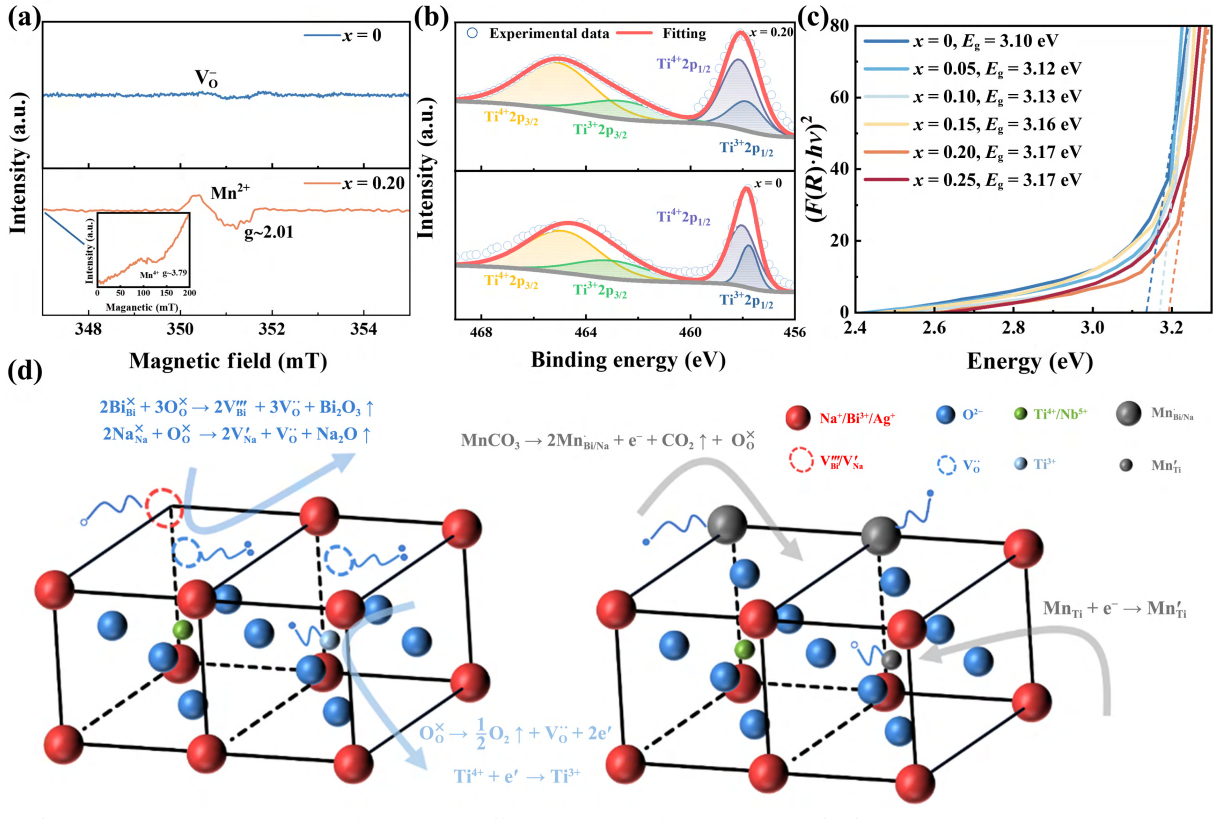

Fig. 4 Defect characterization and mechanism analysis: (a) EPR profiles and (b) high-resolution XPS spectra of Ti for 0.98BNT–0.02AN–x wt% $MnCO_3$ ceramics at x = 0 and 0.20. (c) Optical band gap of 0.98BNT–0.02AN–x wt% $MnCO_3$ ceramics. (d) Schematic diagram of mechanism of Mn ions in BNT lattice.

and orientation of these displacement vectors facilitate a precise differentiation among various nanodomain regions (the selected regions in Fig. 5(d)), including the rhombohedral (R) phase (red regions) and the tetragonal (T) phase (yellow regions). The T phase corresponds to the locally observed domain structure at the atomic scale, which is consistent with the average structure of the non-*R3c* phase refined from the XRD data. This result is highly consistent with the design concept of introducing an antiferroelectric materials to construct polymorphic nanodomains to achieve a high polarization response and a large remanent polarization, wherein the T-phase nanodomains are embedded within the R-phase matrix. Such a coexisting polymorphic domain structure significantly reduces the anisotropy energy and lowers the domain-switching energy barrier, thereby facilitating the rotation and field-induced alignment of the nanodomains [53,54]. Consequently, under an applied external electric field, these polar nanodomains can more easily switch, couple, and irreversibly transform into long-range ferroelectric domains, ultimately yielding an ultrahigh macroscopic remanent polarization upon removal of the electric field. Furthermore, Figs. 5(e) and 5(g) indicate that the system retains an average polarization displacement of approximately 7.80 pm, with localized regions exhibiting displacements exceeding 15 pm, which is beneficial for achieving a high polarization response.

Additionally, through the HAADF-STEM image acquired along the $[110]_p$ crystallographic direction in Fig. 5(a) and the extracted line intensity profile in Fig. 5(b), nonperiodic fluctuations are observed in the A-site cation columns. The two-dimensional (2D) reconstructed atomic column intensity map in Fig. 5(c) further shows their contrast variations. Since the contrast of HAADF-STEM images is highly sensitive to the atomic number (Z), these contrast variations suggest the potential presence of A-site vacancies and defect dipoles [55]. These potential defect dipoles, originating from the coupling between Mn ions and A-site vacancies [56], could act as pinning centers to suppress the destruction of ferroelectric domains under thermal agitation [57]. Consequently, the ferroelectric domains remain stable over a wider temperature range, endowing the 0.98BNT–0.02AN–0.20 wt% $MnCO_3$ ceramic with excellent thermal stability up to 160 °C.

In summary, the ultrahigh remanent polarization of 52.21 μC/cm² and its excellent thermal stability can be attributed to the synergistic effect of composition design and defect engineering. On the one hand, the composition design by introducing the AN phase induces the formation of a polymorphic nanodomain configuration, providing the structural foundation for the ultrahigh remanent polarization. On the other hand, the defect engineering achieved through Mn doping not only enhances the ferroelectricity of the ceramics by suppressing the reduction of Ti^{4+} but also introduces pinning centers that effectively stabilize the macroscopic ferroelectric domain order at high temperatures, protecting it from thermal agitation. It is this synergistic effect that endows the ceramic with outstanding comprehensive performance.

Based on the 0.98BNT–0.02AN–0.20 wt% $MnCO_3$ ceramics, we fabricated multilayer ceramic capacitors (denoted as MLCC-BNT) featuring seven dielectric layers using a tape-casting process. The capacitance at 100 Hz and room temperature is 73.69 nF, with a dielectric loss of 0.0281. The dielectric and electrode layers exhibit dense and uniform microstructures characterized by uniform elemental distribution, and the interfaces are clearly defined and devoid of diffusion layers (Fig. 6(a)). Under an electric field of 12.5 kV/mm, a remanent polarization of 51.17 μC/cm² can be achieved, representing the highest value among currently reported multilayer ceramic capacitors for force–electric energy conversion (Fig. 6(b)). In

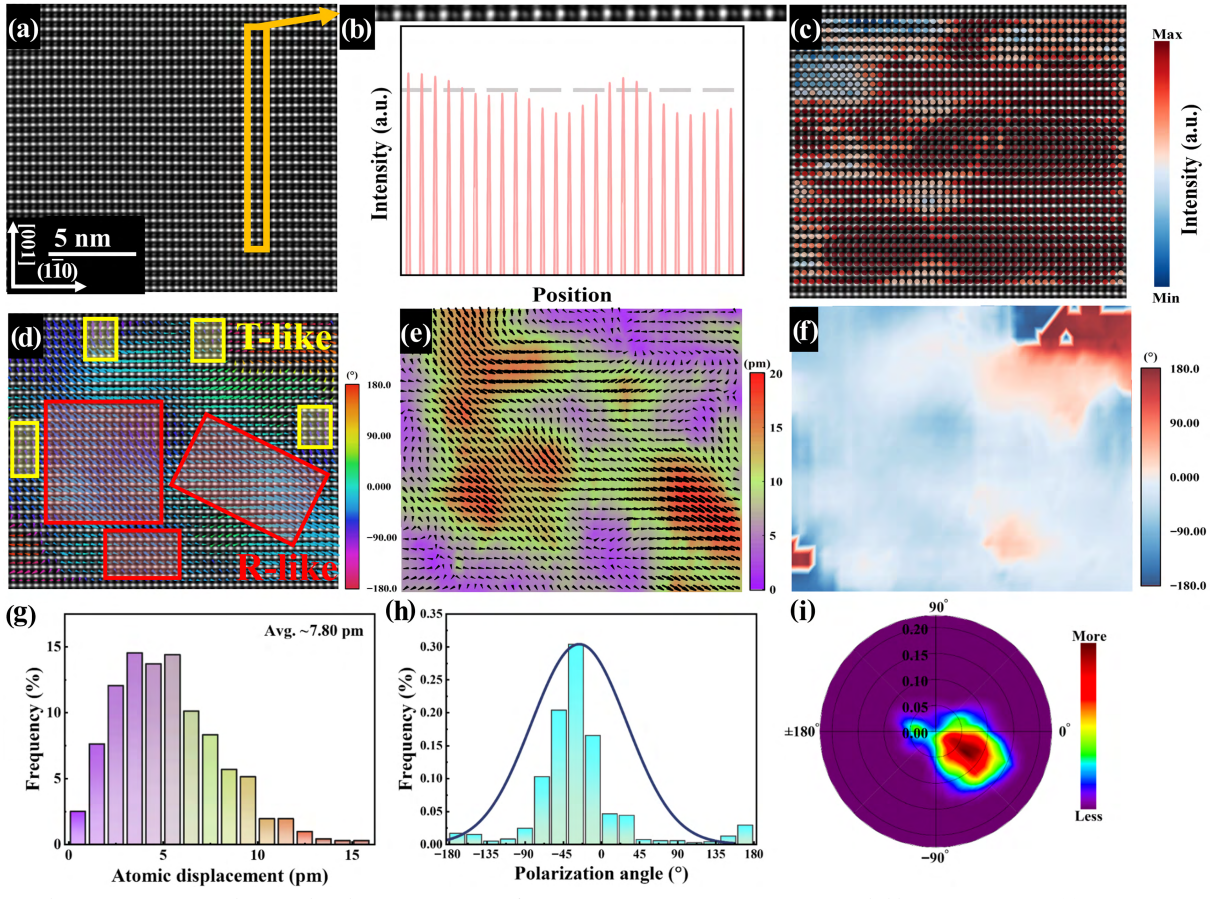

Fig. 5 Local atomic occupancy and nanoscale polarization mapping of 0.98BNT–0.02AN–0.20 wt% $MnCO_3$ revealed by HAADF-STEM: (a) HAADF-STEM image acquired along $[110]_p$ crystallographic direction. (b) Line intensity profile extracted along orange box in (a), corresponding to A-site cation columns. (c) Atomic column intensity map of A-site sublattice reconstructed from (a), visualizing local occupancy variations. (d) HAADF-STEM image acquired along $[110]_p$ crystallographic direction and distribution of polar displacement vector. Distribution mappings of polar displacement (e) magnitudes and (f) angles. Statistical distribution of polar displacements (g) angles and (h) magnitudes. (i) Statistical distribution of the magnitude and angle of the polarization vector.

practical applications, capacitors are frequently subjected to extremely high temperatures. Therefore, the reliability of our MLCC-BNT was rigorously evaluated across a broad temperature range. Under an electric field of 8 kV/mm and in a temperature range of 30–150 °C, the MLCC-BNT demonstrates excellent stability (Fig. 6(c)), maintaining a high P_r. The temperature-dependent *P*–*E* loops of the MLCCs (Fig. 6(c)) exhibit a more pronounced decay in P_r at elevated temperatures compared with the corresponding bulk ceramics (Fig. 3(a)). This discrepancy primarily originates from the thinner dielectric layers (~40 μm) in the MLCCs, which restrict grain growth and result in smaller grain sizes. While these smaller grains facilitate rapid depolarization under stress, they also render the material more susceptible to thermal agitation. Despite this, the MLCCs still maintain reliable ferroelectricity from room temperature up to 150 °C, satisfying the requirements for practical applications. Meanwhile, temperature-dependent dielectric spectra indicate that the depolarization temperature T_d of the MLCCs-BNT is approximately 150 °C (Fig. 6(f)), which further demonstrates the excellent thermal stability of the MLCCs-BNT.

Additionally, the charge released by the MLCC-BNT was collected using rapid thermal depolarization and hydrostatic depolarization devices (Fig. 6(d)). A comparison reveals that, compared with bulk ceramics, MLCCs release charges more easily. This is because the size of the ferroelectric domain is related to the grain size; the grains in MLCC-BNT are smaller than those in bulk ceramics. Under the excitation of an external field, smaller domains can achieve a highly dynamic response, thereby facilitating depolarization [58]. In practical applications, the MLCC-BNT exhibits outstanding force-electric conversion performance. Under the action of a 7 GPa shock wave, a polarization of 49.70 μC/cm² can be released, approaching complete depolarization (Fig. 6(e)). The peak current reaches 90 A, which significantly outperforms reported ferroelectric ceramic devices for ultrahigh-power force-electric energy conversion. These advanced characteristics establish MLCC-BNT as a highly promising candidate for ultrahigh-power force-electric energy conversion.

To explore the phase transition behavior of 0.98BNT–0.02AN–0.20 wt% $MnCO_3$ ceramics in practical applications, the pressure-dependent structural evolution of 0.98BNT–0.02AN–0.20 wt% $MnCO_3$ ceramics under pressures ranging from 0 to 10.0 GPa was investigated using *in situ* Raman spectroscopy. The significant differences between the high- and low-pressure spectra, along with the band broadening and the appearance of new peaks under high pressure, indicate the occurrence of a pressure-induced structural rearrangement [59] (Figs. 7(a) and 7(b)). Upon spectral deconvolution (Fig. 7(c)), the frequency bands can be divided into three main regions [60]: low-frequency region A (< 200 cm^{-1}, translational vibrations of A-site cations), middle-frequency region B (200–400 cm^{-1}, stretching and bending vibrations of Ti–O bonds), and high-frequency region C (> 400 cm^{-1}, breathing and deformation modes of TiO_6 octahedra).

The evolution of the Raman shifts reveals three phase transition

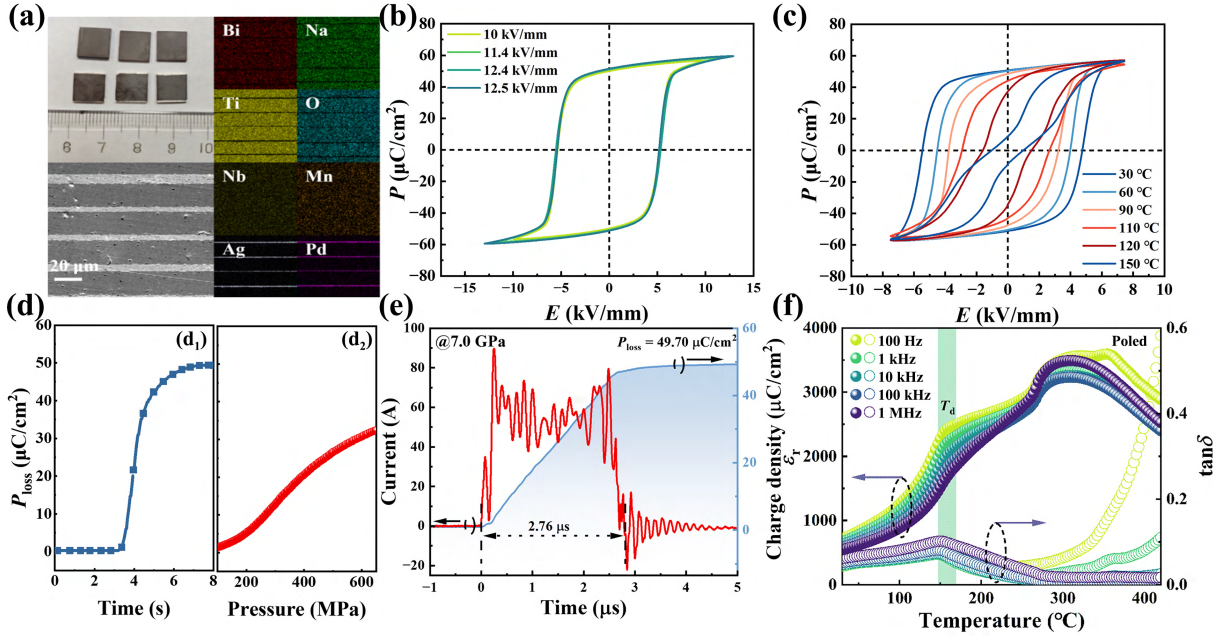

Fig. 6 Microstructure and macroscopic performance of fabricated MLCCs: (a) external morphology, cross-sectional SEM images, and corresponding energy-dispersive X-ray spectroscopy (EDS) elemental mapping. (b) *P*–*E* loops at different electric fields. (c) Temperature-dependent *P*–*E* loops. (d_1) Thermal depolarization curve and (d_2) *in situ* depolarization curve under hydrostatic pressures. (e) Practical dynamic discharge response collected under shock compression. (f) Temperature-dependent dielectric properties.

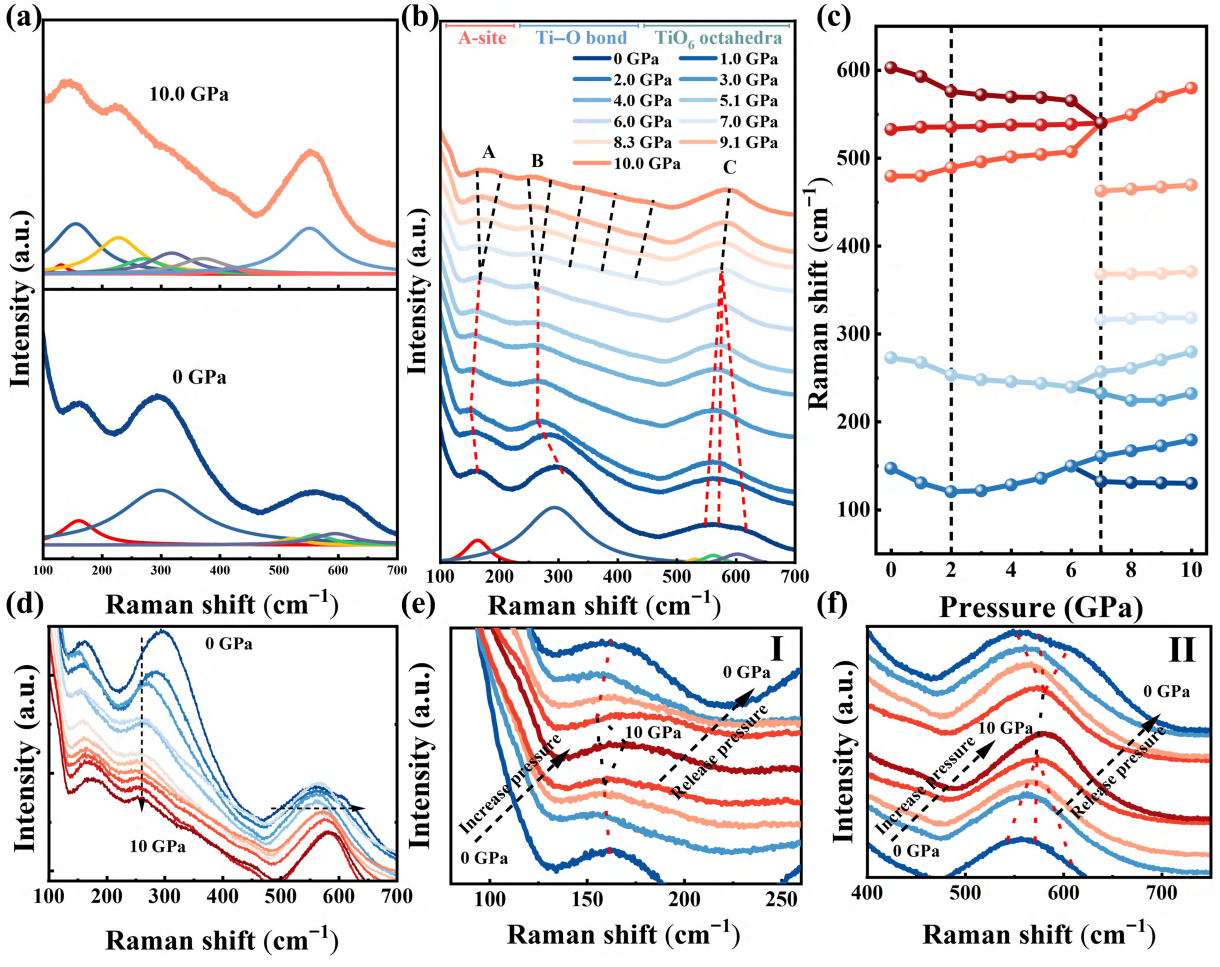

Fig. 7 Pressure-dependent structural evolution of 0.98BNT–0.02AN–0.20 wt% $MnCO_3$ ceramics: (a) Raman spectra and their spectral deconvolutions at 0 and 10.0 GPa. (b) *In situ* Raman spectra as a function of pressure from 0 to 10.0 GPa. (c) Pressure-dependent evolution of deconvoluted Raman peaks. (d) Overlaid *in situ* high-pressure Raman spectra from 0 to 10.0 GPa. (e) Enlarged local view I and (f) enlarged local view II of *in situ* Raman spectra collected during compression and decompression cycle (0–10.0–0 GPa).

stages [59]: (I) 0–2.0 GPa: The polar rhombohedral phase is maintained, but an inflection point appears in band A (~135 cm^{-1}) at approximately 2.0 GPa, indicating a transition of the A-site cation displacement from parallel to $[111]_p$ to parallel to $[100]_p$, which is consistent with the pressure-induced phase transition (~1.5 GPa) observed in previous Raman and XRD studies [3,59]; (II) 2.0–7.0 GPa: An intermediate transition stage characterized by continuous structural adjustment; (III) > 7.0 GPa: The high-frequency modes (band C) merge and exhibit a blueshift, while the middle-frequency region undergoes splitting, resulting in an increased number of Raman-active modes. This is in accordance with the group theory prediction for a transition from the *R3c* phase (13 modes) to the lower-symmetry orthorhombic Pnma phase (24 modes) [60], indicating the disappearance of B-site cation displacement ($[111]_p \rightarrow [000]$) and the evolution of the oxygen octahedral tilt system to $a^-b^+a^-$, marking the complete transformation of the material into a nonpolar orthorhombic structure [59]. Furthermore, as the pressure increases, the low-frequency scattering intensity associated with polar nanoregions (PNRs) in relaxor ferroelectrics decreases sharply (Fig. 7(d)), demonstrating that high pressure effectively suppresses local polar clusters [59]. *In situ* spectra collected during the pressure release process (Figs. 7(e) and 7(f)) confirm that this structural phase transition is macroscopically reversible. In summary, microscopic phonon dynamics confirm that 0.98BNT–0.02AN–0.20 wt% $MnCO_3$ ceramics undergo an evolution from the polar *R3c* phase through an intermediate state to the nonpolar *Pnma* phase under high pressure, revealing their behavior of phase transition-induced depolarization under shock compression (7.0 GPa), thereby enabling the output of high-power current.

4 Conclusions

In summary, through a synergistic composition optimization and defect engineering strategy, we have achieved an ultrahigh remanent polarization (52.21 μC/cm^2, far exceeding those of most lead-free and lead-based ferroelectric materials) and excellent thermal stability in lead-free 0.98BNT–0.02AN–0.20 wt% $MnCO_3$ ferroelectric ceramics. The realization of this exceptional performance is attributed to the enhanced lattice distortion and polymorphic nanodomain structure induced by the AN phase, as well as the defect dipoles formed by Mn ions and vacancies. Notably, we demonstrated the effectiveness of this synergistic strategy in the field of high-power force-electric energy conversion. The fabricated MLCC-BNT achieved a record-breaking peak pulse current of 90 A. Our results demonstrate that a synergistic optimization strategy can significantly enhance the intrinsic ferroelectricity and thermal stability of lead-free BNT-based systems, providing reliable strategic guidance and material support for high-power force-electric energy conversion.

Acknowledgements

This work was supported by the National Natural Science Foundation of China (No. U243020008).

Author contributions

Maocai Xu: writing – original draft, investigation, and formal analysis. Meng Xie: writing – review and editing, methodology, and conceptualization. Min Shi: investigation, methodology (hardware construction). Mingyue Ge: investigation. Shiyu Fang: investigation. Hao Hong: investigation. Tengfei Hu: investigation. Zimeng Hu: validation, writing – proofreading. Fei Cao: methodology (hardware construction). Anwei Sun: formal analysis. Jia Yang: formal analysis. Zhengwei Xiong: resources. Xujie Lv: resources. Zhipeng Gao: resources. Hengchang Nie: writing – review and editing, supervision, resources, funding acquisition, methodology, and conceptualization. Genshui Wang: supervision, resources, funding acquisition, methodology, and conceptualization.

Availability of data and materials

The data that support the findings of this study are available from the corresponding author upon reasonable request.

Competing interests

The authors have no competing interests to declare that are relevant to the content of this article.

Electronic Supplementary Material

Supplementary material is available in the online version of this article at https://doi.org/10.26599/JAC.2026.9221345.

References

[1] Simon P, Gogotsi Y. Materials for electrochemical capacitors. *Nat Mater* 2008, **7**: 845–854.
[2] Altgilbers LL. Explosive pulsed power: An enabling technology. *Acta Phys Pol A* 2009, **115**: 1040–1043.
[3] Yang LT, Kong X, Li F, *et al.* Perovskite lead-free dielectrics for energy storage applications. *Prog Mater Sci* 2019, **102**: 72–108.
[4] Gao ZP, Peng W, Chen B, *et al.* Giant power output in lead-free ferroelectrics by shock-induced phase transition. *Phys Rev Mater* 2019, **3**: 035401.
[5] Nie HC, Yu Y, Liu YS, *et al.* Enhanced shock performance by disperse porous structure: A case study in PZT95/5 ferroelectric ceramics. *J Am Ceram Soc* 2017, **100**: 5693–5699.
[6] Avdeev M, Jorgensen JD, Short S, *et al.* Pressure-induced ferroelectric to antiferroelectric phase transition in $Pb_{0.99}(Zr_{0.95}Ti_{0.05})_{0.98}Nb_{0.02}O_3$. *Phys Rev B* 2006, **73**: 064105.
[7] Lin YZ, Nie HC, Xie M, *et al.* Ultrahigh polarization $Bi_{0.5}Na_{0.5}TiO_3$-based relaxor ceramics for force-electric conversion. *Appl Phys Lett* 2023, **123**: 083903.
[8] Peng P, Nie HC, Liu Z, *et al.* Scaling behavior for $(Bi_{0.5}Na_{0.5})TiO_3$ based lead-free relaxor ferroelectric ceramics. *J Appl Phys* 2017, **122**: 064102.
[9] Peng P, Nie HC, Cheng GF, *et al.* Thermal-induced structural transition and depolarization behavior in $(Bi_{0.5}Na_{0.5})TiO_3$–$BiAlO_3$ ceramics. *J Appl Phys* 2018, **123**: 114102.
[10] Peng P, Nie HC, Liu Z, *et al.* Enhanced ferroelectric properties and thermal stability of Mn-doped $0.96(Bi_{0.5}Na_{0.5})TiO_3$–$0.04BiAlO_3$ ceramics. *J Am Ceram Soc* 2017, **100**: 1030–1036.
[11] Zhang J, Pan Z, Guo FF, *et al.* Semiconductor/relaxor 0–3 type composites without thermal depolarization in $Bi_{0.5}Na_{0.5}TiO_3$-based lead-free piezoceramics. *Nat Commun* 2015, **6**: 6615.
[12] Liu Z, Ren WJ, Nie HC, *et al.* Pressure driven depolarization behavior of $Bi_{0.5}Na_{0.5}TiO_3$ based lead-free ceramics. *Appl Phys Lett* 2017, **110**: 212901.
[13] Chen JQ, Peng P, Lin YD, *et al.* Electrostrain optimization of bismuth sodium titanate-based ceramics by Sm doping. *J Am Ceram Soc* 2025, **108**: 20415.
[14] Luo WQ, Li DX, Li ZP, *et al.* Structure and dielectric energy storage properties of secondary phase $CaCu_3Ti_4O_{12}$ modified BSBNT relaxor ferroelectric ceramics. *Adv Ceram* 2023, **44**: 218–225. (in Chinese)
[15] Liu Z, Lu T, Xue F, *et al.* Lead-free (Ag,K)NbO_3 materials for high-performance explosive energy conversion. *Sci Adv* 2020, **6**: eaba0367.
[16] Tian T F, Chen F L, Zhang L B, *et al.* Advances in energy storage of $AgNbO_3$-based antiferroelectric ceramics. *Adv Ceram* 2023, **44**: 153–172. (in Chinese)
[17] Xu YH, Wang GD, Tian Y, *et al.* Crystal structure and electrical properties of $AgNbO_3$-based lead-free ceramics. *Ceram Int* 2016, **42**: 18791–18797.
[18] Mishra SK, Gupta MK, Mittal R, *et al.* Suppression of

antiferroelectric state in $NaNbO_3$ at high pressure from *in situ* neutron diffraction. *Appl Phys Lett* 2012, **101**: 242907.
[19] Niu X, Jian XD, Chen XY, *et al.* Enhanced electrocaloric effect at room temperature in Mn^{2+} doped lead-free $(BaSr)TiO_3$ ceramics via a direct measurement. *J Adv Ceram* 2021, **10**: 482–492.
[20] Jabeen N, Hussain A, Nawaz S, *et al.* Thermally stable piezoelectric performance of MnO_2 inserted pseudo-tetragonal phase existent $CaBi_2Nb_2O_9$-based ceramics. *Mater Technol* 2022, **37**: 2702–2710.
[21] Wen QL, Guo HH, Shen ZY, *et al.* MnO_2 doping induced structural tuning drives superior piezoelectric response in $CaBi_4Ti_4O_{15}$-based ceramics. *J Adv Ceram* 2025, **14**: 9221051.
[22] Zhao PY, Jiang Y, Wang HX, *et al.* $BaTiO_3$-based multilayer ceramic capacitors with superior stability in energy-storage and pulse properties. *J Adv Ceram* 2026, **15**: 9221264.
[23] Zhao PY, Cai ZM, Wu LW, *et al.* Perspectives and challenges for lead-free energy-storage multilayer ceramic capacitors. *J Adv Ceram* 2021, **10**: 1153–1193.
[24] Wang HX, Zhao PY, Chen LL, *et al.* Energy storage properties of 0.87$BaTiO_3$–0.13$Bi(Zn_{2/3}(Nb_{0.85}Ta_{0.15})_{1/3})O_3$ multilayer ceramic capacitors with thin dielectric layers. *J Adv Ceram* 2020, **9**: 292–302.
[25] Pang QY, Chen Y, Wang ZX, *et al.* Structure, electric, and dielectric properties of $(Sr_{0.7}Ca_{0.3})_{1.02}(Zr_{0.95-x}Ti_{0.05}Mn_x)O_{3+\delta}$ ceramics for BME–MLCCs application. *J Adv Ceram* 2024, **13**: 1382–1393.
[26] Yao JJ, Yang YD, Monsegue N, *et al.* Effect of Mn substituents on the domain and local structures of $Na_{1/2}Bi_{1/2}TiO_3$–$BaTiO_3$ single crystals near a morphotropic phase boundary. *Appl Phys Lett* 2011, **98**: 132903.
[27] Jiang DD, Du JM, Gu Y, *et al.* Evolution of electric response of $Pb_{0.99}(Zr_{0.95}Ti_{0.05})_{0.98}Nb_{0.02}O_3$ and $Pb_{0.99}[(Zr_{0.90}Sn_{0.10})_{0.96}Ti_{0.04}]_{0.98}Nb_{0.02}O_3$ ferroelectric ceramics under shock wave compression. *High Pressure Res* 2012, **32**: 280–290.
[28] Che CY, Bao YZ, Hu ZM, *et al.* Ultrahigh-power-density BNT ferroelectric multilayer ceramic capacitors for pulse power energy conversion components. *J Mater Chem C* 2024, **12**: 16732–16740.
[29] Jo W, Schaab S, Sapper E, *et al.* On the phase identity and its thermal evolution of lead free $(Bi_{1/2}Na_{1/2})TiO_3$–6 mol% $BaTiO_3$. *J Appl Phys* 2011, **110**: 074106.
[30] Jo HR, Lynch CS. Effect of composition on the pressure-driven ferroelectric to antiferroelectric phase transformation behavior of $(Pb_{0.97}La_{0.02})(Zr_{1-x-y}Sn_xTi_y)O_3$ ceramics. *J Appl Phys* 2014, **116**: 074107.
[31] Carl K, Hardtl KH. Electrical after-effects in $Pb(Ti,Zr)O_3$ ceramics. *Ferroelectrics* 1977, **17**: 473–486.
[32] Shkuratov SI, Baird J, Talantsev EF. The depolarization of $Pb(Zr_{0.52}Ti_{0.48})O_3$ ferroelectrics by cylindrical radially expanding shock waves and its utilization for miniature pulsed power. *Rev Sci Instrum* 2011, **82**: 054701.
[33] Zhang SJ, Luo J, Li F, *et al.* Polarization fatigue in $Pb(In_{0.5}Nb_{0.5})O_3$–$Pb(Mg_{1/3}Nb_{2/3})O_3$–$PbTiO_3$ single crystals. *Acta Mater* 2010, **58**: 3773–3780.
[34] Shkuratov SI, Baird J, Antipov VG, *et al.* Multilayer PZT 95/5 antiferroelectric film energy storage devices with giant power density. *Adv Mater* 2019, **31**: 1904819.
[35] Maqbool A, Hussain A, Rahman JU, *et al.* Composition-dependent structural, dielectric and ferroelectric responses of lead-free $Bi_{0.5}Na_{0.5}TiO_3$–$SrZrO_3$ ceramics. *J Korean Phys Soc* 2016, **68**: 1430–1438.
[36] Parija B, Badapanda T, Panigrahi S, *et al.* Ferroelectric and piezoelectric properties of $(1-x)(Bi_{0.5}Na_{0.5})TiO_3$–$xBaTiO_3$ ceramics. *J Mater Sci—Mater El* 2013, **24**: 402–410.
[37] Bai WF, Li LY, Li W, *et al.* Phase diagrams and electromechanical strains in lead-free BNT-based ternary perovskite compounds. *J Am Ceram Soc* 2014, **97**: 3510–3518.
[38] Ng YS, Alexander SM. Structural studies of manganese stabilised lead-zirconate-titanate. *Ferroelectrics* 1983, **51**: 81–86.
[39] Ma C, Guo HZ, Beckman SP, *et al.* Creation and destruction of morphotropic phase boundaries through electrical poling: A case study of lead-free $(Bi_{1/2}Na_{1/2})TiO_3$–$BaTiO_3$ piezoelectrics. *Phys Rev Lett* 2012, **109**: 107602.
[40] Levin I, Reaney IM. Nano- and mesoscale structure of $Na_{1/2}Bi_{1/2}TiO_3$: A TEM perspective. *Adv Funct Mater* 2012, **22**: 3445–3452.
[41] Du G, Liang RH, Wang L, *et al.* Large stable strain memory effect in poled Mn-doped $Pb(Mn_{1/3}Sb_{2/3})O_3$–$Pb(Zr,Ti)O_3$ ceramics. *Appl Phys Lett* 2013, **102**: 162907.
[42] Ohshima Y, Ochiai Y, Takagi Y, *et al.* Control of structural phase transition and energy storage behavior through cooling rate in $(Bi_{0.5}Na_{0.5})TiO_3$–$BaTiO_3$ ceramics. *Appl Phys Lett* 2025, **126**: 012908.
[43] Wang SM, Qian J, Ge GL, *et al.* Embedding plate-like pyrochlore in perovskite phase to enhance energy storage performance of BNT-based ceramic capacitors. *Adv Energy Mater* 2025, **15**: 2403926.
[44] Ge GL, Qian J, Xu K, *et al.* Excellent energy storage performance of polymorphic modulated antiferroelectric lead zirconate ceramic. *Adv Mater* 2025, **37**: 2505731.
[45] Zhao L, Liu Q, Zhang SJ, *et al.* Lead-free $AgNbO_3$ anti-ferroelectric ceramics with an enhanced energy storage performance using MnO_2 modification. *J Mater Chem C* 2016, **4**: 8380–8384.
[46] Wilkinson DT, Crane HR. Precision measurement of the *g* factor of the free electron. *Phys Rev* 1963, **130**: 852–863.
[47] Xu CH, Fu ZQ, Liu Z, *et al.* La/Mn codoped $AgNbO_3$ lead-free antiferroelectric ceramics with large energy density and power density. *ACS Sustain Chem Eng* 2018, **6**: 16151–16159.
[48] Peng JH, Nie HC, Yuan YO, *et al.* Enhanced ferroelectric properties in $BiAlO_3$ modified lead-free Mn-doped $Bi_{0.5}(Na_{0.8}K_{0.2})_{0.5}TiO_3$ thin films. *Int J Appl Ceram Tec* 2024, **21**: 3645–3651.
[49] Lobacheva O, Yiu YM, Chen N, *et al.* Changes in local surface structure and Sr depletion in Fe-implanted $SrTiO_3$ (001). *Appl Surf Sci* 2017, **393**: 74–81.
[50] Orel ZC, Gunde MK, Orel B. Application of the Kubelka–Munk theory for the determination of the optical properties of solar absorbing paints. *Prog Org Coat* 1997, **30**: 59–66.
[51] Li D, Lin Y, Zhang M, *et al.* Achieved ultrahigh energy storage properties and outstanding charge–discharge performances in $(Na_{0.5}Bi_{0.5})_{0.7}Sr_{0.3}TiO_3$-based ceramics by introducing a linear additive. *Chem Eng J* 2020, **392**: 123729.
[52] Nie XR, Jing RY, Chen FK, *et al.* Synergistic phase boundary and defect engineering enables ultrahigh electrostrain in lead-free ceramics. *Adv Funct Mater* 2026, **36**: 13360.
[53] Yang YL, Liu ZY, Ren PR, *et al.* Modulation of phase boundary and domain structures to engineer strain properties in BNT-based ferroelectrics. *J Adv Ceram* 2024, **13**: 967–975.
[54] Yin J, Shi XM, Tao H, *et al.* Deciphering the atomic-scale structural origin for large dynamic electromechanical response in lead-free $Bi_{0.5}Na_{0.5}TiO_3$-based relaxor ferroelectrics. *Nat Commun* 2022, **13**: 6333.
[55] Xu GY, Zhong Z, Bing Y, *et al.* Electric-field-induced redistribution of polar nano-regions in a relaxor ferroelectric. *Nat Mater* 2006, **5**: 134–140.
[56] Cen ZY, Bian SS, Xu Z, *et al.* Simultaneously improving piezoelectric properties and temperature stability of $Na_{0.5}K_{0.5}NbO_3$ (KNN)-based ceramics sintered in reducing atmosphere. *J Adv Ceram* 2021, **10**: 820–831.
[57] Tian S, Xin JP, Cheng Y, *et al.* Strong pinning effect on domains in piezoelectrics. *Acta Mater* 2024, **280**: 120344.
[58] Li S, Hu TF, Nie HC, *et al.* Giant energy density and high efficiency achieved in silver niobate-based lead-free antiferroelectric ceramic capacitors via domain engineering. *Energy Storage Mater* 2021, **34**: 417–426.
[59] Kreisel J, Glazer AM, Bouvier P, *et al.* High-pressure Raman study of a relaxor ferroelectric: The $Na_{0.5}Bi_{0.5}TiO_3$ perovskite. *Phys Rev B* 2001, **63**: 174106.
[60] Kreisel J, Glazer AM, Jones G, *et al.* An X-ray diffraction and Raman spectroscopy investigation of A-site substituted perovskite compounds: The $(Na_{1-x}K_x)_{0.5}Bi_{0.5}TiO_3$ ($0 \le x \le 1$) solid solution. *J Phys—Condens Mat* 2000, **12**: 3267–3280.